


Shape coexistence in neutron-deficient ^{188}Hg investigated via lifetime measurements

M. Siciliano ^{1,2,3,*}, I. Zanon,^{1,2,4} A. Goasduff,^{2,5,6} P. R. John,^{2,5,7} T. R. Rodríguez,⁸ S. Péru,⁹ I. Deloncle,^{9,10} J. Libert,⁹ M. Zielńska,³ D. Ashad,¹¹ D. Bazzacco,⁵ G. Benzoni,¹² B. Birkenbach,¹³ A. Boso,^{2,5} T. Braunroth,¹³ M. Cicerchia,^{1,2} N. Cieplicka-Oryńczak,^{12,14} G. Colucci,^{2,5,15} F. Davide,¹¹ G. de Angelis,¹ B. de Canditiis,¹¹ A. Gadea,¹⁶ L. P. Gaffney,¹⁷ F. Galtarossa,^{1,4} A. Gozzelino,¹ K. Hadyńska-Klęk,^{1,15} G. Jaworski,^{1,15} P. Koseoglou,⁷ S. M. Lenzi,^{2,5} B. Melon,¹⁸ R. Menegazzo,⁵ D. Mengoni,^{2,5} A. Nannini,¹⁸ D. R. Napoli,¹ J. Pakarinen,¹⁹ D. Quero,¹¹ P. Rath,¹¹ F. Recchia,^{2,5} M. Rocchini,¹⁸ D. Testov,^{2,5,20} J. J. Valiente-Dobón,¹ A. Vogt,¹³ J. Wiederhold,⁷ and W. Witt⁷

¹INFN, Laboratori Nazionali di Legnaro, I-35020 Legnaro, Italy

²Dipartimento di Fisica e Astronomia, Università di Padova, I-35131 Padova, Italy

³Irfu/DPhN/CEA, Université de Paris-Saclay, F-91191 Gif-sur-Yvette, France

⁴Dipartimento di Fisica e Scienze della Terra, Università di Ferrara, I-44121 Ferrara, Italy

⁵INFN, Sezione di Padova, I-35131 Padova, Italy

⁶Department of Physics, University of Warsaw, PL-02-093 Warsaw, Poland

⁷Institut für Kernphysik der Technischen Universität Darmstadt, D-64289 Darmstadt, Germany

⁸Departamento de Física Teórica and Centro de Investigación Avanzada en Física Fundamental, Universidad Autónoma de Madrid, E-28049 Madrid, Spain

⁹CEA, DAM, DIF, F-91297 Arpajon, France

¹⁰IJCLab CNRS/IN2P3, Université de Paris-Saclay, F-91400 Orsay, France

¹¹Dipartimento di Fisica and INFN Sezione di Napoli, I-80126 Napoli, Italy

¹²INFN, Sezione di Milano, I-20133 Milano, Italy

¹³Institut für Kernphysik, Universität zu Köln, D-50937 Cologne, Germany

¹⁴Institute of Nuclear Physics, Polish Academy of Sciences, PL-31-342 Cracow, Poland

¹⁵Heavy Ion Laboratory, University of Warsaw, PL-02-093 Warsaw, Poland

¹⁶Instituto de Física Corpuscular, CSIC-Universidad de Valencia, E-46100 Valencia, Spain

¹⁷University of the West of Scotland, Paisley PA1 2BE, Scotland, United Kingdom

¹⁸Dipartimento di Fisica and INFN Sezione di Firenze, I-50019 Firenze, Italy

¹⁹Fysiikan laitos, Jyväskylän Yliopisto, FI-40014 Jyväskylä, Finland

²⁰Joint Institute for Nuclear Research, RU-141980 Dubna, Russia



(Received 22 February 2020; accepted 2 July 2020; published 22 July 2020)

Background: Shape coexistence in the $Z \approx 82$ region has been established in mercury, lead, and polonium isotopes. For even-even mercury isotopes with $100 \leq N \leq 106$ multiple fingerprints of this phenomenon are observed, which seems to be no longer present for $N \geq 110$. According to a number of theoretical calculations, shape coexistence is predicted in the ^{188}Hg isotope.

Purpose: The aim of this work was to measure lifetimes of excited states in ^{188}Hg to infer their collective properties, such as the deformation. Extending the investigation to higher-spin states, which are expected to be less affected by band-mixing effects, can provide additional information on the coexisting structures.

Methods: The ^{188}Hg nucleus was populated using two different fusion-evaporation reactions with two targets, ^{158}Gd and ^{160}Gd , and a beam of ^{34}S provided by the Tandem-ALPI accelerator complex at the Laboratori Nazionali di Legnaro. The channels of interest were selected using the information from the Neutron Wall array, while the γ rays were detected using the GALILEO γ -ray spectrometer. Lifetimes of excited states were determined using the recoil-distance Doppler-shift method, employing the dedicated GALILEO plunger device.

Results: Lifetimes of the states up to spin $16\hbar$ were measured and the corresponding reduced transition probabilities were calculated. Assuming two-band mixing and adopting, as done commonly, the rotational model, the mixing strengths and the deformation parameters of the unperturbed structures were obtained from the experimental results. In order to shed light on the nature of the observed configurations in the ^{188}Hg nucleus, the extracted transition strengths were compared with those resulting from state-of-the-art beyond-mean-field calculations using the symmetry-conserving configuration-mixing approach, limited to axial shapes, and the five-dimensional collective Hamiltonian, including the triaxial degree of freedom.

Conclusions: The first lifetime measurement for states with spin ≥ 6 suggested the presence of an almost spherical structure above the 12^+ isomer and allowed elucidating the structure of the intruder band. The

* marco.siciliano@lnl.infn.it

comparison of the extracted $B(E2)$ strengths with the two-band mixing model allowed the determination of the ground-state band deformation. Both beyond-mean-field calculations predict coexistence of a weakly deformed band with a strongly prolate-deformed one, characterized by elongation parameters similar to those obtained experimentally, but the calculated relative position of the bands and their mixing strongly differ.

DOI: [10.1103/PhysRevC.102.014318](https://doi.org/10.1103/PhysRevC.102.014318)

I. INTRODUCTION

The regions close to $Z = 50$ and $Z = 82$ provide unique conditions to study the evolution of nuclear shapes and of collectivity in the vicinity of magic numbers. The lead region, in particular, presents a wide range of phenomena related to the nuclear shape, as for instance shape staggering between odd- and even-mass nuclei [1,2], shape evolution with mass [3–5], and shape coexistence [6,7]. The latter is a characteristic feature of finite many-body quantum systems, such as the atomic nucleus, where structures corresponding to different shapes coexist within a similar excitation energy.

The first hint of shape coexistence in the $Z \approx 82$ region came from studies of optical hyperfine structure in the neutron-deficient mercury isotopes [8]. As shown in Fig. 1 (top panel), significant staggering of the mean-square charge radius was observed for mass $181 \leq A \leq 185$, which was interpreted as resulting from the presence of two structures characterized by different deformation. This behavior of mean-square charge radii is unique in the nuclear chart. Recent laser-spectroscopy measurements [2] demonstrated that the shape staggering is present down to $A = 179$ ($N = 99$), where the nucleus returns to sphericity in its ground state.

Another fingerprint of shape coexistence in the mercury isotopes is the observation of low-lying intruder bands built on second 0^+ states, which are particularly close in energy to the ground state in the isotopes from ^{180}Hg to ^{188}Hg [see Fig. 1 (bottom panel)]. From level energies within the bands, the deformations of these nuclei in the ground-state bands were estimated to be $\beta_2 \approx 0.1$, in contrast to $\beta_2 \approx 0.3$ obtained for the bands built on the 0_2^+ states [11,12]. These structures tend to mix due to their proximity in energy. The degree of their mixing was first estimated from the measured α -decay hindrance factors, yielding a 3% admixture of the deformed configuration in the ground state of ^{180}Hg , while mixing of 16% and 18% was obtained for ^{182}Hg and ^{184}Hg , respectively [13]. These admixtures are consistent with those deduced from the $\rho^2(E0; 0_2^+ \rightarrow 0_1^+)$ value for ^{188}Hg and its upper limit for ^{186}Hg [14], and together they display a parabolic behavior as a function of neutron number with maximum mixing observed at the $N = 104$ midshell, where the intruding structure comes the closest in energy to the ground state. The mixing of normal and intruder structures in Hg isotopes was also investigated by applying a phenomenological two-band mixing model to level energies in the observed rotational bands [15,16]. The most recent study [16] took into account the energies of newly identified non-yrast states in $^{180,182}\text{Hg}$ and yielded a lower mixing between the 0^+ states than that deduced from the α -decay work of Ref. [13], but still with a maximum around $N = 102$ – 104 . The conclusions of this analysis [16] for the 2^+ states are, however, much different,

suggesting an inversion of configurations of the 2_1^+ state between ^{182}Hg and ^{184}Hg , with an almost maximum mixing strength (51%) for the 2_1^+ state in the midshell ^{184}Hg nucleus. As for the 0^+ states, when moving away from $N = 104$, both towards lighter and heavier nuclei, the configurations of the 2^+ states become more pure. The importance of configuration mixing in the structure of 2^+ states in neutron-deficient Hg nuclei is further supported by enhanced $\rho^2(E0; 2_2^+ \rightarrow 2_1^+)$ transition strengths observed for ^{180}Hg [17], ^{182}Hg [18], ^{184}Hg [18], and ^{186}Hg [19,20]. Finally, the mixing of states with $J > 2$ extracted from the perturbation of level energies in rotational bands in $^{180-188}\text{Hg}$ [16] decreases with spin and it no longer displays a parabolic behavior as a function of neutron number, but rather a monotonic increase with mass (e.g., for the 4^+ states the admixtures increase from 2% in ^{180}Hg to 20% in ^{188}Hg). Currently, no $E0$ transition strengths are known in neutron-deficient Hg nuclei between the states of spin 4 and higher.

Further information on collective structures in neutron-deficient Hg nuclei was provided by measurements of γ -ray transition strengths. Lifetimes of excited states were measured for several neutron-deficient species, populated via fusion-evaporation reactions: the ^{178}Hg [21], $^{180,182}\text{Hg}$ [22,23], and $^{184,186}\text{Hg}$ [16,24,25] nuclei were studied using the recoil-distance Doppler-shift (RDDS) method, while the Doppler-shift attenuation method (DSAM) and the β -tagged fast-timing (FT) techniques were employed to investigate the ^{184}Hg [26] and $^{186,188}\text{Hg}$ [14,27] isotopes, respectively. Moreover, the lifetimes of low-lying states in $^{190-196}\text{Hg}$ isotopes, which could not be obtained via RDDS method due to the presence of low-lying isomers, were recently measured via the FT technique [27,28]. These studies were mostly limited to yrast states but, as the intruder band becomes yrast at low spin [see Fig. 1 (bottom panel)], they yielded lifetimes of states in both coexisting bands in the even-mass $^{180-186}\text{Hg}$ nuclei, providing strong support for the very different deformations of these two structures.

Finally, with the advent of radioactive ion-beam facilities, the even-mass $^{182-188}\text{Hg}$ isotopes were investigated via low-energy Coulomb excitation, yielding magnitudes and signs of the reduced $E2$ matrix elements between the low-lying excited states [29,30]. Combined with the mixing coefficients of Ref. [16], these results provided a consistent picture of two distinct configurations (weakly deformed oblate and strongly deformed prolate) contributing in varying proportions to the observed low-lying states in $^{182-188}\text{Hg}$. Even though the simplest observables, such as the energy of the first-excited 2^+ state and the $B(E2; 2_1^+ \rightarrow 0_1^+)$ value, are almost identical in $^{182-188}\text{Hg}$, the structures of 2_1^+ states were demonstrated to be very different: the intruder configuration dominates in ^{182}Hg ,

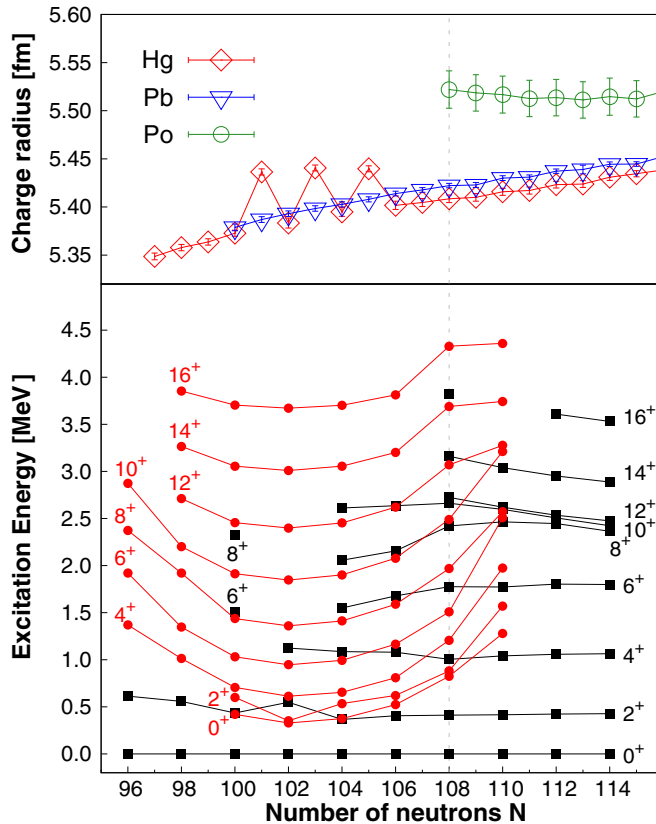


FIG. 1. (Top) Mean-square charge radius as a function of the neutron number for Po (green), Pb (blue), and Hg (red) isotopic chains. For the $Z = 80$ isotopes, the large variation of the radius was attributed to the presence of different shapes. The values are taken from Refs. [2,8,9]. (Bottom) Energy systematics of excited states in the neutron-deficient even-even mercury isotopes, showing (red circles) the assumed intruder and (black squares) ground-state bands. Data extracted using the NNDC On-Line Data Service from the ENSDF database, file revised as of June 2018 [10].

both configurations almost equally contribute in ^{184}Hg , and the normal configuration prevails for $^{186,188}\text{Hg}$. Unfortunately, due to strong correlations between the reduced matrix elements, the important role of $E0$ transitions between the 2^+ states and the lack of sufficiently precise lifetimes, branching and mixing ratios for the nuclei of interest, it was not possible to determine any spectroscopic quadrupole moments from this study, except for the $Q_2(2^+) = 0.8^{+0.5}_{-0.3}$ eb in ^{188}Hg , consistent with an oblate deformation of this state.

The first interpretation of the intruder band was given in the work of Praharaaj and Khadkikar [31], who performed Hartree-Fock calculations for even-mass mercury isotopes from $A = 184$ to $A = 204$ and obtained β_2 deformation parameters for the two coexisting structures. In their calculations, all these nuclei present oblate ground-state bands, with a maximum of the deformation for $A = 186$ ($\beta_2 = 0.117$), while the excited bands are prolate deformed. In particular, small mixing was predicted between the two bands in ^{188}Hg . More recently, Nikšić and collaborators performed relativistic Hartree-Bogoliubov (RHB) calculations [32] and predicted

the ground-state band of Hg isotopes to be weakly deformed oblate, due to the two-proton hole in the $Z = 82$ shell. For the isotopes close to the neutron midshell, including ^{188}Hg , this oblate ground-state band was predicted to be crossed by an intruding prolate-deformed band, related to $4p-6h$ proton excitations into the $h_{9/2}$ and $f_{7/2}$ orbitals, and the two structures were expected to be strongly mixed. Similar conclusions could also be reached from beyond-mean-field (BMF) and interacting-boson model (IBM) calculations that were summarized in the works of Bree *et al.* [29] and Wrzosek-Lipska *et al.* [30]. In these works, the BMF approach predicts for $N \geq 106$ a weakly deformed ground-state band coexisting with an excited prolate band characterized by a stronger deformation. For nuclei with $100 \leq N \leq 104$ the two bands cross and the ground state is expected to be predominantly prolate, while the first excited 0^+ state is predicted to have equal contributions of the oblate and the prolate configuration.

The intruder structure of ^{188}Hg appears at excitation energy slightly higher than in $^{182-186}\text{Hg}$ and it becomes yrast starting from spin 6^+ , where the two bands cross. The degree of mixing between the two coexisting structures is expected to be lower than at midshell, but the detailed predictions of the models significantly differ. As ^{188}Hg is less exotic and thus more accessible for high-precision spectroscopy than the mercury isotopes in the nearest vicinity of $N = 104$, the paucity of information about its electromagnetic structure, in particular that of higher-spin states, is surprising. The transition probabilities in ^{188}Hg were studied via lifetime measurements using the FT technique [14,27] and via Coulomb excitation [29,30]. However, the existing information is mostly limited to yrast states and the results on the 2^+ lifetime are not consistent. In order to obtain a clear picture of shape coexistence in ^{188}Hg and a deeper insight into configuration mixing in Hg nuclei, precise determination of the reduced transition probabilities between the low-lying states, belonging to both structures, is mandatory.

In the present paper, the lifetime measurement of the excited states in both the ground-state and intruder bands in ^{188}Hg is presented. The results are discussed and interpreted in the context of new beyond-mean-field calculations performed via the symmetry-conserving configuration-mixing and the five-dimensional collective Hamiltonian methods.

II. EXPERIMENTAL DETAILS

Two experiments were performed, using different fusion-evaporation reactions, to populate the excited states in ^{188}Hg . In the first one, a ^{34}S beam at 185 MeV energy impinged on a $600 \mu\text{g}/\text{cm}^2$ thick target of ^{160}Gd , evaporated onto a $2.5 \text{ mg}/\text{cm}^2$ thick ^{181}Ta foil. The second one used a ^{34}S beam at the energy of 165 MeV and a $600 \mu\text{g}/\text{cm}^2$ thick target of ^{158}Gd evaporated on an identical foil. In both experiments, the targets were oriented such that the beams first passed through the Ta foils before striking the target material. In the following, these two measurements will be referred to as Expt. 1 and Expt. 2, respectively. As the cross sections for individual reaction channels were different for Expt. 1 and Expt. 2, this approach provided a better control of possible contamination of the ^{188}Hg data by other reaction channels. The ^{34}S

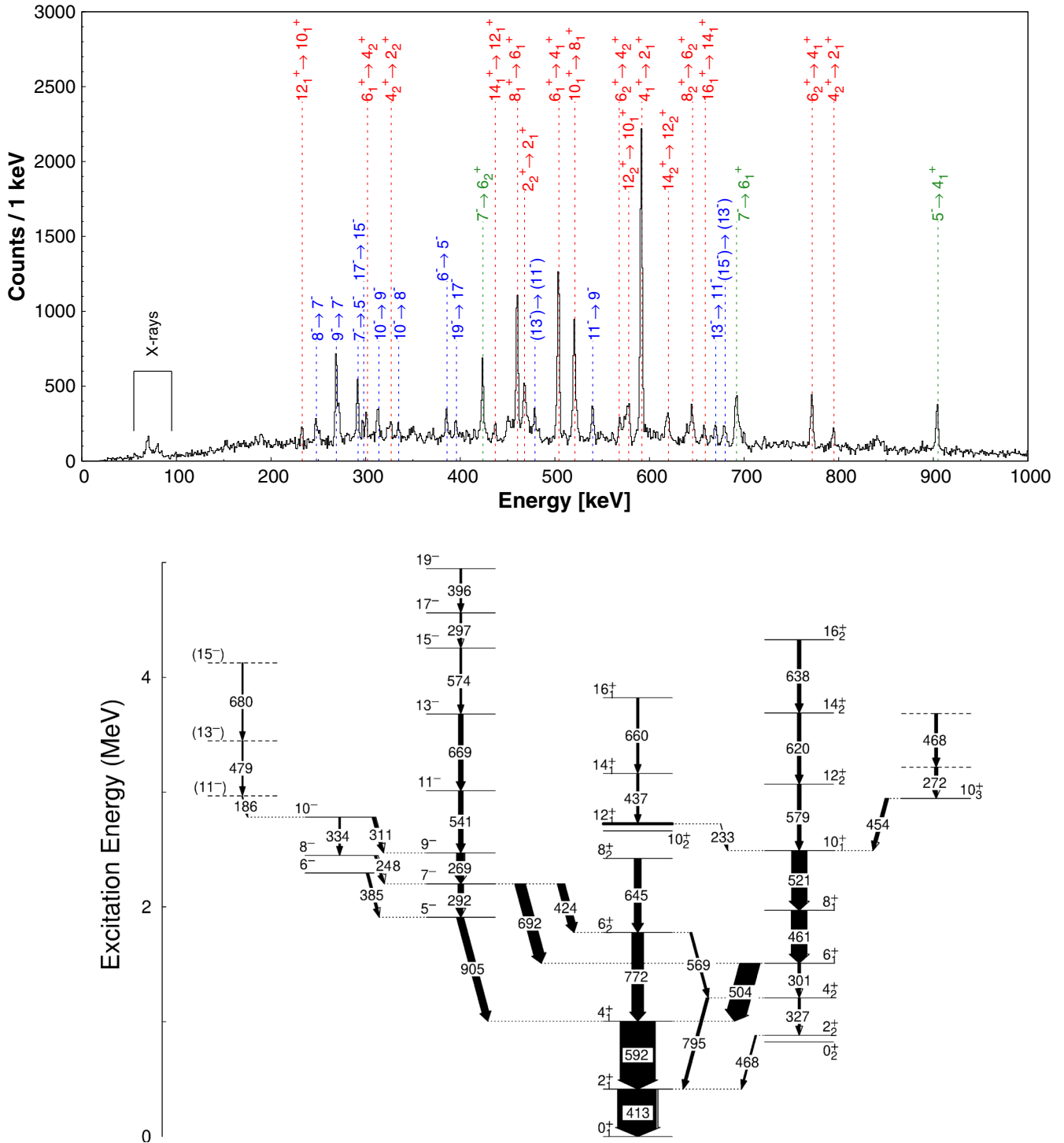


FIG. 2. (Top) Background-subtracted γ -ray energy spectrum from the GALILEO detectors at 90° , obtained by gating on the 413 keV $2_1^+ \rightarrow 0_{g.s.}^+$ transition and requiring the coincidence with at least one neutron. The statistics is the sum of the Expt. 1 and Expt. 2 data sets. The identified transitions in the ^{188}Hg positive-parity bands are marked in red, those in and between negative-parity bands are highlighted in blue, while those between positive-parity and negative-parity bands are in green. (Bottom) Partial level scheme of ^{188}Hg , reporting the γ -ray transitions observed in the present measurement. The arrow widths represent the efficiency-corrected transition yields.

beam was provided by the Tandem-ALPI accelerator complex [33,34] of the Laboratori Nazionali di Legnaro (Italy). The γ rays resulting from the reactions were detected by the GALILEO spectrometer, an array of 25 Compton-shielded

HPGe detectors, arranged into three rings at backward angles (152° , 129° , 119°) and one ring at 90° [35] with respect to the beam direction. The neutrons evaporated in the reaction were detected using the Neutron Wall array [36], composed of 45

liquid scintillators placed at forward angles with respect to the beam direction. The use of Neutron Wall was necessary to discriminate between the events of interest, expected in coincidence with at least one neutron, and the Coulomb-excitation background [37]. Figure 2 (top panel) shows the γ -ray energy spectrum of ^{188}Hg , obtained in coincidence with at least one neutron and gated on the $2_1^+ \rightarrow 0_{g.s.}^+$ transition in ^{188}Hg , summing up the statistics of the two experiments. The contributions of the different data sets can be estimated by comparing the efficiency-corrected intensity of the $2_1^+ \rightarrow 0_{g.s.}^+$ transition in the neutron-gated singles γ -ray energy spectra, which is equal to 1.4×10^7 and 2.4×10^7 for Expt. 1 and Expt. 2, respectively. The partial level scheme, showing all γ -ray transitions observed in the present study, is presented in the bottom panel of Fig. 2. More details about the presorting of the data can be found in Ref. [38].

For the lifetime measurements, the RDDS technique [39] was used by employing the GALILEO plunger [40] with a 11 mg/cm^2 thick ^{197}Au stopper mounted after the target. For each γ -ray transition two components were observed, related to the radiation emitted before and in the ^{197}Au foil: the γ rays emitted in flight after the target are Doppler shifted, while those emitted after the implantation in the stopper are detected at the proper energy. From the energy difference between the in-flight and the stopped components of the γ -ray transitions, the average velocity of the ^{188}Hg evaporation residue (ER) was determined, being $\beta = 1.71(8)\%$ for Expt. 1 and $\beta = 1.59(1)\%$ in Expt. 2. Considering the velocity of the nucleus of interest, seven target-stopper distances in the range 20–600 μm were used during Expt. 1 and seven in the range 7–2000 μm during Expt. 2, to measure lifetimes between few and tens of picoseconds. Specifically, in the first experiment the distances were optimized to get information mostly on the 2_1^+ excited state, while for the second they were selected to extend the measurement also to shorter-lived states.

III. LIFETIME ANALYSIS

In order to avoid the effects of unobserved feeding transitions and to reduce the possibility of contamination from different reaction channels, the lifetime measurements were performed using the γ - γ coincidence procedure, gating on the in-flight component of the most intense feeding transition. Moreover, in order to discriminate against the events resulting from the Coulomb excitation of both ^{197}Au stopper and ^{181}Ta target fronting, all analyzed γ - γ matrices were constructed by requiring the coincidence with at least one neutron identified in the Neutron Wall array. Figure 3 shows the evolution of the intensities of the in-flight and stopped peaks of the $2_1^+ \rightarrow 0_{g.s.}^+$ transition as a function of the target-degrader distance, after gating on the $4_1^+ \rightarrow 2_1^+$ in-flight component. The lifetimes of the states were extracted using the NAPATAU software [41], applying the differential decay curve method (DDCM) [39] by fitting the area of both the in-flight (I_i^{if}) and the stopped (I_i^{st}) components with a polynomial piecewise function. These intensities were scaled according to an external normalization, given by the area of the 136-keV γ -ray peak of ^{181}Ta , coming from the Coulomb excitation of the target fronting. This choice for the normalization was due to the fact that the

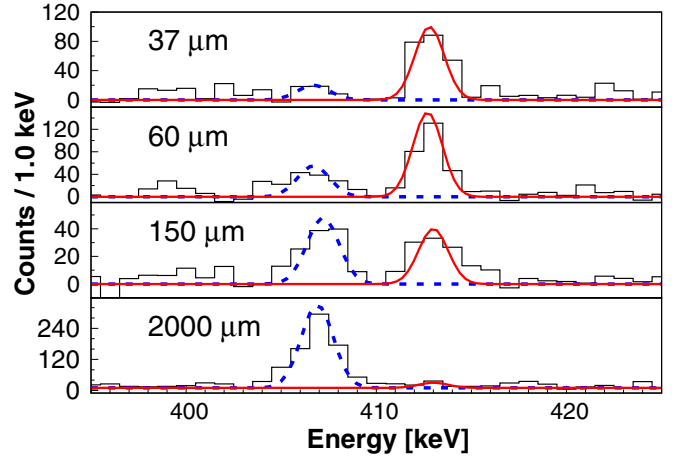


FIG. 3. Background-subtracted γ -ray energy spectra of ^{188}Hg for different target-to-stopper distances for the Expt. 2 data set and the GALILEO detectors at 152° . The spectra are expanded in the vicinity of the $2_1^+ \rightarrow 0_1^+$ transition and obtained by gating on the in-flight component of the $4_1^+ \rightarrow 2_1^+$ transition and requiring the coincidence with at least one neutron. The in-flight and stopped components are indicated by dashed blue and solid red lines, respectively.

number of counts in this peak is not only proportional to the beam intensity and duration of the run, but it also provides a measure of possible degradation of the target during the experiment.

The lifetime τ_i should be the same for each i th target-stopper distance and it is obtained as

$$\tau_i = \frac{I_i^{st} - \sum_j (Br \alpha I_i^{st})_j}{\frac{d}{dt} I_i^{if}}, \quad (1)$$

where the summation is extended over the j feeding transitions, each with a certain branching ratio (Br) and parameter α , which includes the efficiency correction and the angular correlation between the transition of interest and the feeding one. In the case of the γ - γ coincidence procedure with gating on the in-flight component of the feeding transition, the contributions from feeding transitions are eliminated and this term is null. The final result is given by the weighted average of the lifetimes within the sensitive region of the technique, i.e., where the derivative of the fitting function is largest.

The lifetimes of the $J^\pi = 2_1^+, 4_1^+, 6_1^+, 8_1^+, 10_1^+, 14_1^+$, and 16_1^+ excited states in ^{188}Hg were extracted via the DDCM by gating on the in-flight component of the $(J+2)^\pi \rightarrow J^\pi$ feeding transition. The lifetimes of these states were obtained using data for each of the three GALILEO rings separately and then the weighted averages were calculated, except for the 16^+ state where in order to obtain sufficient statistics data from the three rings had to be summed. In Fig. 4 the DDCM analysis performed for the 2_1^+ state is presented for Expt. 1 and Expt. 2, showing the results for the detectors at 129° and 152° , respectively. The lifetimes obtained from the two experiments and data from the three HPGe rings are in a good agreement. Thus, the weighted averages of the results obtained for the different detector angles were calculated, leading to $\tau(2_1^+) = 25(2)$ ps for Expt. 1, $\tau(2_1^+) = 24(1)$ ps for Expt. 2. The

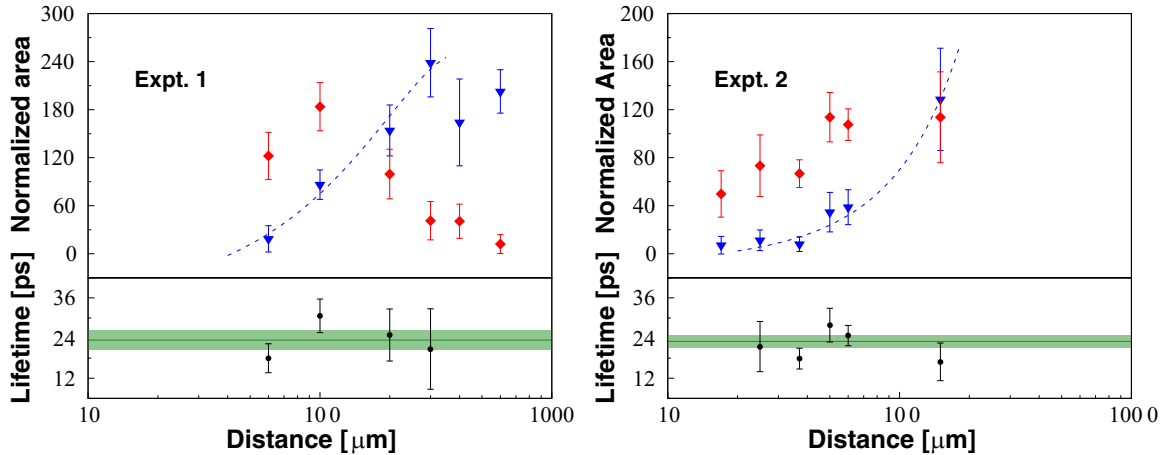


FIG. 4. DDCM analysis for the lifetime measurement of the 2_1^+ excited state, after gating on the in-flight component of the $4_1^+ \rightarrow 2_1^+$ transition. (Top) Area of the in-flight (blue) and stopped (red) components, normalized to the area of the 136-keV γ -ray peak of ^{181}Ta . The dashed lines represent a fit to the in-flight-component points in the sensitive region of the technique. (Bottom) Corresponding lifetimes obtained for individual distances. The solid line denotes the weighted average of the lifetimes, while the filled area corresponds to 1σ uncertainty.

lifetime of the 4_1^+ state could be determined only from the Expt. 2 data set, which yielded $\tau(4_1^+) = 1.9(8)$ ps. These results are in agreement with those given in the literature [27,29,30].

The stopped components of the γ -ray decays from the 12_2^+ state were observed only at the two shortest distances employed in Expt. 2, implying a very short lifetime for the 12_2^+ state. Using these two data points, a lifetime of ≈ 2 ps was extracted, which would yield a transitional quadrupole moment consistent with the trend observed for the high-spin members of the intruder band (see discussion in Sec. IV). However, due to an insufficient number of experimental points in the sensitive range of the method, we adopt a more conservative upper limit of 4 ps for this state.

The presence of the 154-ns 12_1^+ isomeric state prevented the investigation of the $J^\pi = 10_2^+, 8_2^+, 6_2^+$ states with the RDDS technique. From the Expt. 1 and Expt. 2 measurements, an upper limit of 10 ps can be set for the 6_2^+ excited state, since in the spectra gated on both the 645-keV $8_2^+ \rightarrow 6_2^+$ and the 424-keV $7^- \rightarrow 6_2^+$ transitions only the in-flight component of the $6_2^+ \rightarrow 4_1^+$ transition was observed clearly for the data obtained for the longer plunger distances.

Due to the insufficient level of statistics for the in-flight component of the 301-keV $6_1^+ \rightarrow 4_2^+$ transition, it was not possible to extract the lifetime of the 4_2^+ state via the DDCM. Thus, for the Expt. 2 data set, a gate on the 460-keV $8_1^+ \rightarrow 6_1^+$ transition was set and the lifetime was extracted via the decay-curve method (DCM), using a second-order Bateman equation and taking into account the lifetime of the 6_1^+ state. Figure 5 shows the decay curve for the 4_2^+ state, resulting in a lifetime of $\tau(4_2^+) = 8(3)$ ps.

Table I summarizes the experimental results from the two data sets. The reported uncertainties represent the 1σ statistical error, given by the adopted procedures and the weighted average of the results from the individual GALILEO rings. Additionally, a systematic uncertainty (typically $\leq 3\%$), accounting for the choice of the fitting function and relativistic effects [39], should be considered. Because of the lack of

shorter distances investigated in Expt. 1, it was possible to study the lifetimes of the 2_1^+ , 6_1^+ , and 14_1^+ excited states only. Similar to the 6_2^+ case discussed above, only an upper limit can be set for the 4_2^+ and 16_1^+ states.

IV. DISCUSSION

From the weighted average of lifetimes ($\bar{\tau}$) measured in Expt. 1 and Expt. 2, the corresponding $B(E2)$ values can be extracted, which can be related to the deformation parameters using simple rotational approximations. In the axially symmetric rotor model, the transitional quadrupole moment Q_t is related to the $E2$ transition probability via

$$B(E2; J_i \rightarrow J_f) = \frac{5}{16\pi} \langle J_i, K, 2, 0 | J_f, K \rangle^2 Q_t^2, \quad (2)$$

where $J_f = J_i - 2$ and $\langle J_i, K, 2, 0 | J_f, K \rangle$ is the Clebsch-Gordan coefficient. K is the spin projection along the symmetry axis of the nucleus, conserved in the case of axial symmetry (thus it is equal to 0 for the considered states in both coexisting structures in ^{188}Hg). Under this assumption,

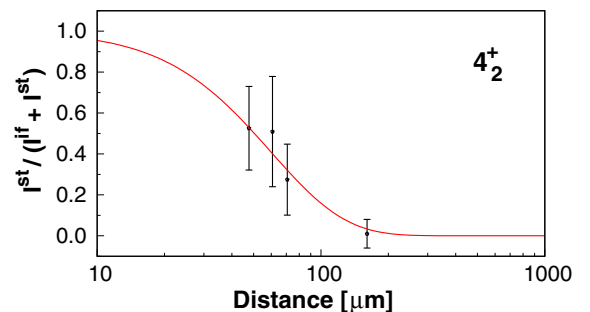


FIG. 5. Decay curve of the 4_2^+ excited state in ^{188}Hg as a function of the target-stopper distance, obtained for the Expt. 2 data set by gating on the in-flight component of the $8_1^+ \rightarrow 6_1^+$ transition (see text). The red line represents the fitted decay curve, assuming $\tau(6_1^+) = 5.1(5)$ ps.

TABLE I. Lifetimes (in picoseconds) of the J_i^π excited states in ^{188}Hg . The weighted averages of the results from the three GALILEO rings are given and compared with the literature values [27,29,30]. The reported uncertainties are statistical only.

| J_i^π | Expt. 1 | Expt. 2 | Literature |
|-----------|---------|---------|------------|
| 2_1^+ | 25(2) | 24(1) | 19(3) |
| 4_1^+ | – | 1.9(8) | 2.3(2) |
| 4_2^+ | <10 | 8(3) | <58 |
| 6_1^+ | 5.5(6) | 5.1(5) | <14 |
| 6_2^+ | <10 | <10 | <30 |
| 8_1^+ | – | 2.7(2) | – |
| 10_1^+ | – | 2.1(2) | – |
| 12_2^+ | – | <4 | – |
| 14_1^+ | 18(4) | 19(3) | – |
| 16_1^+ | <20 | 12(3) | – |

Q_t does not change within a band and it is equal to the intrinsic quadrupole moment Q_0 , which is related to the β_2 deformation parameter via

$$Q_0 = \frac{3}{\sqrt{5\pi}} ZR_0^2 \beta_2 (1 + 0.36\beta_2), \quad (3)$$

where $R_0 = 1.20A^{1/3}$.

In Table II the $B(E2)$ values and the corresponding Q_t and β_2 values are reported for the in-band transitions. Based on the excitation energies of the states and the Q_t values, three different configurations can be identified: a slightly deformed ground-state structure below the 12_1^+ isomeric state, an almost spherical structure above it, and finally the deformed intruder band. For the latter, within the experimental uncertainties, the quadrupole moments tend to be constant for the $4 \leq J \leq 10$ states. This observation is consistent with relatively low mixing between the ground-state and intruder bands. Indeed, according to Ref. [16], the ground-state and excited

bands present almost pure configurations with admixtures below 7%, with an exception of the 4^+ states, where this value increases to $\approx 20\%$. This suggests that in-band transition probabilities are only weakly affected by the mixing, leading to a rather constant trend of the quadrupole moments. Consequently, a first estimate of reduced transition probabilities in the pure intruder structure can be obtained using the average Q_t value for the $4 \leq J \leq 10$ states ($Q_t \approx 5.88$ eb, which corresponds to $\beta_2 \approx 0.21$). We note here that the nature of the 10_1^+ state may be different, as it will be discussed in Sec. IV A, but as the corresponding Q_t value agrees within experimental uncertainties with those for lower-spin members of the band, it has been included in the average.

Since there is substantial experimental evidence for the mixing between the ground-state and the intruder bands [e.g., significant $\rho^2(E0)$ values, intense interband transitions], it is reasonable to assume that the two structures are not axially symmetric. Thus, following a similar procedure as for the axial-rotor case, one can assume that the $J \geq 4$ intruder states result from a rotation of a nonaxial nucleus characterized by two deformation parameters (β_2, γ). Consequently, the measured $B(E2)$ values can be related to the intrinsic quadrupole moment Q_0 using the following extension of Eq. (2), as proposed, for example, in Ref. [43]:

$$B(E2; J \rightarrow J-2) = \frac{5}{8\pi} Q_0^2 \frac{J(J-1)}{(2J-1)(2J+1)} \times \left[\cos(\gamma + 30^\circ) - \frac{\langle K^2 \rangle}{(J-1)J} \cos(\gamma - 30^\circ) \right]^2. \quad (4)$$

Applying the described model to the measured $B(E2)$ values for $4 \leq J \leq 10$, one obtains for the pure intruder configuration $Q_0 = 5.90(22)$ eb [corresponding to $\beta_2 = 0.21(1)$] and $\gamma = 14(2)^\circ$. Here, it is again assumed $K = 0$ for all states in the intruder band, as the departure from axial symmetry is

TABLE II. Comparison between the reduced transition probabilities $B(E2; J_i^\pi \rightarrow J_f^\pi)$, extracted from the measured lifetimes, and the theoretical values predicted by 5DCH and SCCM for ^{188}Hg . The transitional quadrupole moment Q_t and the β_2 deformation parameter are extracted assuming an axially symmetric rotor model. The experimental values marked with ^(a) and the branching ratios (Br) are taken from Ref. [42].

| $J_i^\pi \rightarrow J_f^\pi$ | E_γ [keV] | $\bar{\tau}$ [ps] | Br | $B(E2 \downarrow)$ [W.u.] | | | $ Q_t $ [eb] | β_2 |
|-------------------------------|------------------|-------------------------------|-----------|---------------------------|------|------|----------------------|---------------------|
| | | | | Expt. | 5DCH | SCCM | | |
| $2_1^+ \rightarrow 0_1^+$ | 413 | 24.4(9) | 1.00 | 42 (2) | 82 | 60 | 3.66(10) | 0.128(4) |
| $4_1^+ \rightarrow 2_1^+$ | 592 | 1.9(8) | 1.00 | 91_{-27}^{+66} | 109 | 94 | 4.5_{-7}^{+14} | 0.158_{-26}^{+49} |
| $6_2^+ \rightarrow 4_1^+$ | 772 | <10 | 0.77(2) | >3.6 | 22 | 113 | >0.85 | >0.03 |
| $12_1^+ \rightarrow 10_2^+$ | 62 | ^(a) 222(29) 10^3 | 1.00(1) | 1.3(2) | – | – | 0.49(5) | 0.017(2) |
| $14_1^+ \rightarrow 12_1^+$ | 437 | 19(3) | 1.00 | 40(6) | – | – | 2.73(31) | 0.095(11) |
| $16_1^+ \rightarrow 14_1^+$ | 660 | 12(3) | 1.00 | 8.4_{-17}^{+28} | – | – | 1.24_{-13}^{+19} | 0.043_{-4}^{+7} |
| $4_2^+ \rightarrow 2_2^+$ | 327 | 8(3) | 0.46(2) | 178_{-53}^{+118} | 215 | 316 | 6.33_{-103}^{+183} | 0.229_{-8}^{+19} |
| $6_1^+ \rightarrow 4_2^+$ | 301 | 5.3(3) | 0.175(12) | 154(14) | 295 | 355 | 5.60(35) | 0.196(12) |
| $8_1^+ \rightarrow 6_1^+$ | 461 | 2.7(2) | 1.00 | 220(17) | 347 | 382 | 6.56(35) | 0.229(12) |
| $10_1^+ \rightarrow 8_1^+$ | 521 | 2.1(2) | 1.00 | 155(15) | 330 | – | 5.42(37) | 0.189(13) |
| $12_2^+ \rightarrow 10_1^+$ | 579 | <4 | 1.00 | >48 | – | – | >3.00 | >0.105 |
| $2_2^+ \rightarrow 0_1^+$ | 881 | ^(a) 203(45) | 0.58(6) | 0.068_{-18}^{+28} | 0.2 | 0.4 | – | – |
| $6_1^+ \rightarrow 4_1^+$ | 504 | 5.3(3) | 0.779(14) | 56(3) | 13 | 1.5 | – | – |

not large and K is likely to be approximately a good quantum number.

In order to shed light on the nature of the coexisting structures, accounting for the mixing between them, the experimental reduced transition probabilities are further compared with a band-mixing model [44] and with beyond-mean-field calculations.

A. Two-band mixing

The assumption of a purely rotational character of the high-spin intruder states is in line with the work of Gaffney *et al.* [16] where, considering a spin-independent interaction between two rotational structures and employing the method of Ref. [44], the mixing amplitude (α_{mix}) for the excited states up to spin $10\hbar$ were extracted from the excitation energies. The 6_1^+ , 8_1^+ , and 10_1^+ excited states were estimated to have admixture of the normal structure at the level of 6.1%, 1.2%, and 0.5%, respectively.

By applying the two-band mixing (TBM) model [44] to the transition probabilities determined from the presently measured lifetimes, information on the pure normal and intruder configurations can be obtained. Indeed, such a two-state mixing model is a simple approach to interpret the properties of physical states based on the mixing of different intrinsic configurations. As extensively discussed in the work of Cl  ment *et al.* [45], the experimentally observed states $|J_{1,2}^\pi\rangle$ can be written as a linear combination of the intrinsic pure prolate ($|J_{pr}^\pi\rangle$) and oblate states ($|J_{ob}^\pi\rangle$):

$$\begin{aligned} |J_1^\pi\rangle &= \alpha_{\text{mix}}|J_{ob}^\pi\rangle + \sqrt{1 - \alpha_{\text{mix}}^2}|J_{pr}^\pi\rangle \\ |J_2^\pi\rangle &= -\sqrt{1 - \alpha_{\text{mix}}^2}|J_{ob}^\pi\rangle + \alpha_{\text{mix}}|J_{pr}^\pi\rangle, \end{aligned} \quad (5)$$

where the pure structures are assumed to be orthogonal but their mixing gives rise to the observed interband transitions.

Based on the excitation energy of the states belonging to the ground-state and intruder bands (see Fig. 2), it seems that only the $J \leq 8$ levels should be considered when applying the two-band mixing model. Indeed, in the ground-state band the rotational-like pattern is maintained up to the 8_2^+ state, while the 10_2^+ state has an energy so close to that of the 12_2^+ isomer that it seems to belong to a different configuration. In the intruder band, instead, the 10_1^+ state is fed by a 456-keV transition from another 10^+ level, so one cannot exclude the possibility of it being mixed with this third structure. Thus, for the $J \leq 8$ states one can estimate the deformation of the unperturbed configurations from the experimental $B(E2; J \rightarrow J-2)$ values, adopting the mixing strengths of Ref. [16], phenomenologically derived from the excitation energies of both yrast and non-yrast states. The resulting normal structure is characterized by $|Q_0^n| = 3.67(37)$ eb ($\beta_2 \approx 0.13$) and the intruder one by $|Q_0^i| = 6.41(43)$ eb ($\beta_2 \approx 0.22$). The reduced transition probabilities, corresponding to the unperturbed and mixed structures, are compared with the experimental results in Fig. 6: while for the $4_1^+ \rightarrow 2_1^+$ and $4_2^+ \rightarrow 2_2^+$ transitions the large uncertainty does not allow us to make any conclusion on the mixing, the strengths of the $2_1^+ \rightarrow 0_{g.s.}^+$, $6_1^+ \rightarrow 4_2^+$, and $8_1^+ \rightarrow 6_1^+$ transitions confirm the estimated

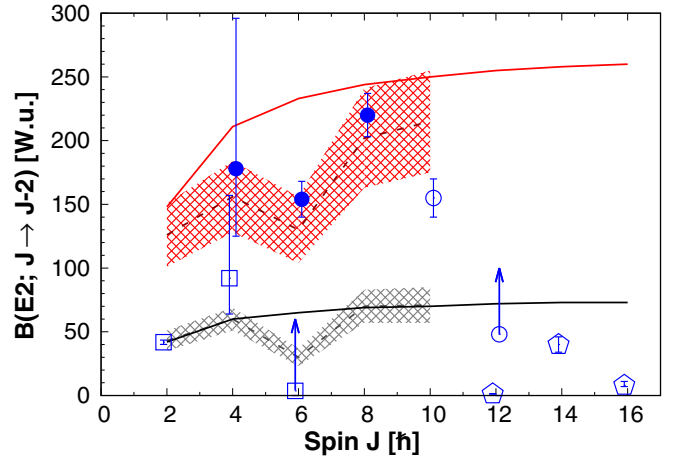


FIG. 6. Measured $B(E2)$ values as a function of spin are compared with those calculated from the two-band mixing model [44]. The black (red) solid line denotes unperturbed normal (intruder) structures transition strengths, obtained for an axial rotor with $Q_0^n = 3.67$ eb ($Q_0^i = 6.41$ eb). Assuming the mixing amplitudes of Ref. [16], the gray (red) dashed line represents the $B(E2)$ values for ground-state (excited) band, while the related shaded areas correspond to their error bars. The experimental values are presented with open squares for the ground-state band, with solid circles for the $J < 10$ states of the intruder band, with an open circle for the $J \geq 10$ state of the intruder band (see text) and with open pentagons for the almost spherical band above the 12_1^+ isomer.

α_{mix} of Ref. [16]; on the other hand, the disagreement between the $B(E2; 10_1^+ \rightarrow 8_1^+)$ value and the prediction for the unperturbed intruder structure supports the hypothesis previously discussed, suggesting a more complex nature of the 10^+ states that goes beyond the two-band mixing model.

The same procedure can also be applied to the known $B(E2)$ values in the even-mass $^{180-186}\text{Hg}$ [16,22,24–26,29,30], yielding a systematic evaluation of the quadrupole moments for the unperturbed configurations. The obtained quadrupole moments, presented in Fig. 7 (TBM-3), exhibit a parabolic behavior with a maximum for ^{182}Hg ($|Q_0^n| = 4.15$ eb and $|Q_0^i| = 8.63$ eb). This trend reflects the evolving collectivity while moving away from the neutron midshell and it is consistent with the excitation energy systematics shown in Fig. 1.

In Ref. [16] (TBM-1) and Ref. [30] (TBM-2), the quadrupole moments of the unperturbed configurations are extracted by adopting the two-band mixing approach with the same mixing amplitudes, but under different assumptions. Gaffney and collaborators [16] assumed the transitional quadrupole moments of the coexisting structures to be spin dependent, given by the average of the moments of inertia of the initial and final states. The resulting Q_0 values are rather constant as a function of the mass number, while they obviously increase with spin. This effect is stronger for the ground-state bands, where the Q_0^n values of the high-spin states (i.e., $J^\pi = 8^+, 10^+$) can exceed by over a factor of 2 those of low-spin states (i.e., $J^\pi = 2^+, 4^+$), see Fig. 7. In contrast, the excited bands exhibit a slower increase of Q_0^i with spin. This difference can be attributed to the paucity of experimental information on the ground-state bands, which

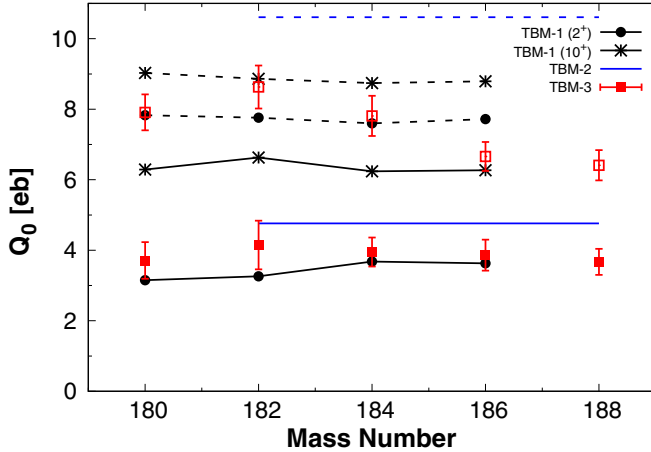


FIG. 7. Systematics of $|Q_0^n|$ (solid lines and filled squares) and $|Q_0^i|$ (dashed lines and open squares), derived from different variants of the two-band mixing approach. TBM-1 assumes spin-dependent quadrupole moments for the two unperturbed configurations [16]. For clarity, only those for 2^+ and 10^+ states are plotted. TBM-2 postulates that the coexisting configurations are the same in all even-mass $^{182-188}\text{Hg}$ isotopes [30]. TBM-3 considers for each isotope different prolate and oblate configurations, whose quadrupole moments are spin independent (see text).

was limited to the $B(E2; 2_1^+ \rightarrow 0_{g.s.}^+)$ values, and/or to a more robust character of the deformed configuration. In the work of Wrzosek-Lipska *et al.* [30], instead, the two-band mixing approach was implemented by postulating that the unperturbed configurations are the same in all even-mass $^{182-188}\text{Hg}$ isotopes. The Q_0^n and Q_0^i values were fitted to the $E2$ matrix elements coupling the 0^+ and 2^+ states obtained from Coulomb excitation of $^{182-188}\text{Hg}$. The resulting quadrupole moments, which supersede those reported in the work of Bree *et al.* [29], are $|Q_0^n| = 4.76$ eb for the normal configuration and $|Q_0^i| = 10.61$ eb for the intruder one. While the estimate for the normal configuration is similar to those of TBM-1 and TBM-3, it yields a considerably larger quadrupole moment for the intruder configuration, probably due to the choice of the experimental information that has been taken into account in this evaluation. Moreover, as the $^{182-186}\text{Hg}$ nuclei lie closer to the $N = 104$ neutron midshell, they are expected to be more collective than ^{188}Hg , so this procedure may lead to an overestimation of the quadrupole moments in the latter.

B. Beyond-mean-field calculations

In view of the measured lifetimes, many of them obtained for the first time, the neutron-deficient $^{186,188,190}\text{Hg}$ have been studied within a self-consistent beyond-mean-field framework [46,47], i.e., the five-dimensional collective Hamiltonian (5DCH) [48] and the symmetry-conserving configuration mixing (SCCM) [49,50] methods, with the Gogny-D1M [51] and Gogny-D1S [52,53] interactions, respectively. These calculations are based on the mixing of a set of intrinsic states with different quadrupole deformations.

In the 5DCH approach, the intrinsic states are obtained by constrained Hartree-Fock-Bogolyubov calculations (CHFB)

performed for around 90 points in the (β_2, γ) plane, defined by $0 \leq \beta_{2,\text{max}} \leq 0.8$ and $0^\circ \leq \gamma \leq 60^\circ$. These calculations are performed using a triaxial harmonic oscillator basis including 13 major shells, which is a sufficiently large model space to ensure the energy convergence. The overlap of the intrinsic states is assumed to be Gaussian: the Gaussian-overlap approximation (GOA) allows us to derive from the Hill-Wheeler equation a Bohr-type Hamiltonian, called the 5DCH. This Hamiltonian deals with quadrupole degrees of freedom only, thus two vibrations and three rotations are taken into account. The 5DCH potential term is determined by the CHFB energy, obtained at the different (β_2, γ) deformation points, to which the zero-point energies are added. The kinetic terms involving three mass parameters and three rotational inertia parameters are also deduced from CHFB solutions.

In the SCCM approach, the intrinsic states are Hartree-Fock-Bogoliubov (HFB)-like wave functions obtained self-consistently through the particle-number variation after projection (PN-VAP) method [54]. Because the HFB states also break the rotational invariance of the system, this symmetry is restored by projecting onto good angular momentum [particle-number and angular momentum projection (PNAMP)]. The final spectrum and nuclear wave functions are obtained by mixing such PNAMP states within the generator coordinate method (GCM). The region under study is expected to show competing shapes in the low-lying spectrum. Such kind of system can be particularly sensitive to the convergence of the calculations with the number of harmonic oscillator shells, $N_{h.o.}$, used to define the HFB transformation [55].

Initially the SCCM calculations were performed with $N_{h.o.} = 11$ including triaxial shapes with the result that the prolate band was predicted to be the ground-state configuration, contrary to what is obtained experimentally. Consequently, exploratory SCCM calculations limited to the axial quadrupole (β_2) degree of freedom were performed for $N_{h.o.} = 11, 13, 15,$ and 17 . A strong dependence of the excitation energies of the less-deformed band was observed as a function of $N_{h.o.}$, with the inversion of the bands disappearing for larger bases. On the other hand, the β_2 deformation of the two structures was almost independent on the number of harmonic oscillator shells: $\beta_2 \approx 0.20$ for the oblate-deformed configuration and $\beta_2 \approx 0.25$ for the prolate one. Only for $N_{h.o.} = 17$ convergence was obtained for the energies and wave functions. Such a large number of harmonic oscillator shells makes the SCCM with triaxial shapes extremely expensive from the computational point of view and, consequently, only axial SCCM results with $N_{h.o.} = 17$ are reported here.

A first estimation of the structure of the $^{186,188,190}\text{Hg}$ isotopes can be obtained by analyzing the calculated energy surfaces as a function of deformation parameters. Figure 8 presents the PN-VAP and PNAMP energies, calculated within the SCCM approach, as a function of the deformation β_2 . For each of the three nuclei two clear minima are present, corresponding to oblate ($\beta_2 \approx -0.17$) and prolate superdeformed (SD) ($\beta_2 \approx +0.65$) shapes, and a double minimum structure around normal-deformed (ND) prolate configurations with $\beta_2 \approx +0.1, +0.3$. Once the angular momentum projection is performed, in the three cases, the absolute minimum for $J = 0$

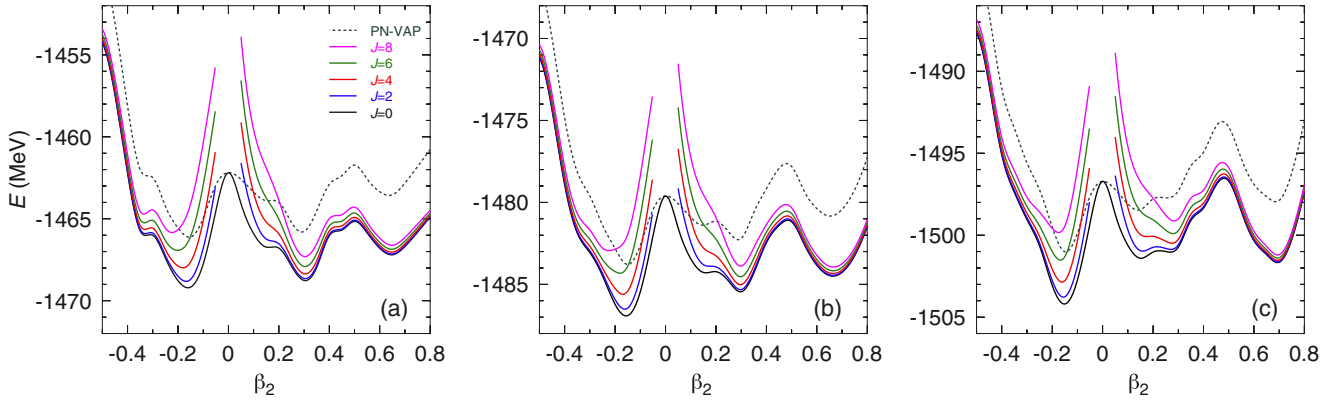


FIG. 8. PN-VAP (dashed lines) and PNAMP (continuous lines) energy curves as a function of the axial quadrupole deformation β_2 for the (a) ^{186}Hg , (b) ^{188}Hg , and (c) ^{190}Hg isotopes. The results are obtained with the Gogny-D1S interaction within the SCCM approach.

is the oblate one, then the ND configuration and, finally, the SD one. Oblate and ND minima are rather close in energy in ^{186}Hg , while ND and SD minima are almost degenerate in ^{190}Hg .

Similar conclusions can be drawn from the analysis of the potential-energy surfaces (PES) for $^{186,188,190}\text{Hg}$ (see Fig. 9), serving as a basis for the 5DCH approach. For ^{188}Hg , the oblate minimum with $\beta_2 \approx 0.16$ is the deepest one, followed by a slightly more shallow prolatelike deformed minimum with a significant degree of triaxiality $(\beta_2, \gamma) = (0.28, 13^\circ)$, and finally an axial prolate-superdeformed minimum with $\beta_2 \approx 0.65$, which is predicted much higher in energy. The PES for ^{186}Hg is very similar, with the only difference that the two ND minima are almost degenerate. On the contrary, for ^{190}Hg the prolatelike normal-deformed minimum disappears, while the SD prolate minimum becomes more pronounced, in line with the conclusions of Ref. [56]. One can clearly conclude that the energy surfaces resulting from both calculations suggest the presence of shape coexistence in these nuclei.

As already mentioned, the final theoretical spectra are obtained by mixing intrinsic HFB-like states having different quadrupole deformations. In the SCCM calculations, the GCM is applied to mix the PNAMP states. In the 5DCH approach, the intrinsic CHFBS states are mixed assuming a Gaussian overlap to solve the GCM-equivalent equation.

Figure 10 shows the excitation energies, obtained with the SCCM approach, for the $^{186,188,190}\text{Hg}$ nuclei as a function of the mean value of the intrinsic quadrupole deformation for each state provided by the collective wave functions (CWF). Here, we clearly observe for the three isotopes the three different collective bands (with $\Delta J = 2$) associated to the oblate (ground-state bands), ND-prolate and SD-prolate minima. The excitation energy of the 0_2^+ state in ^{186}Hg is lower than those for $^{188,190}\text{Hg}$, as observed experimentally. For ^{190}Hg , the 0_2^+ state is found close to the band head of the SD band.

Figure 11 presents a comparison of the partial level scheme of ^{188}Hg with the theoretical spectra, calculated within the SCCM and 5DCH approaches. Although the absolute minimum of the PES in Fig. 9 is located at an oblate deformation, the oblatelike (band A) and prolatelike (band B) structures resulting from the 5DCH calculations are inverted with respect to experimental data. Nevertheless, the energy difference between the two 0^+ states is 674 keV, which is similar to what is observed experimentally, and suggests that mixing between the two structures may be correctly reproduced. In contrast, while the SCCM calculation reproduces the proper ordering of the bands, it predicts a much larger excitation energy of the 0_2^+ state, which can be related to the absence of the triaxial degree of freedom and result in a smaller mixing between

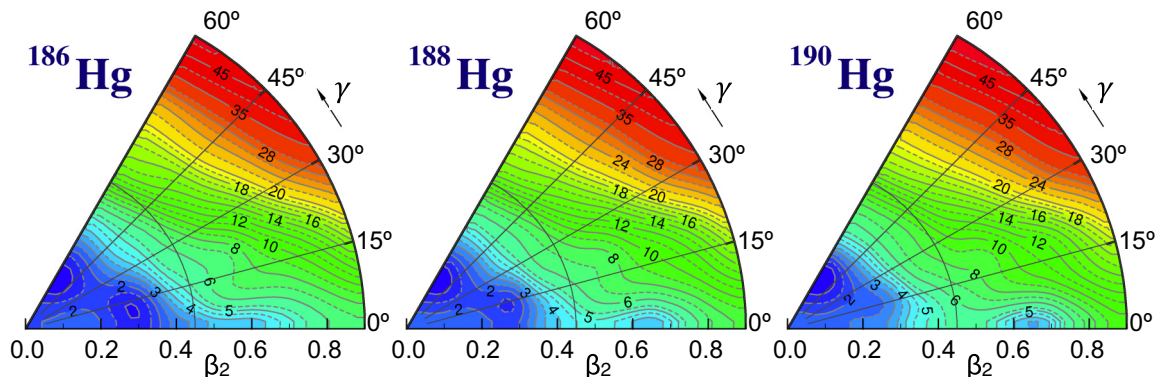


FIG. 9. Potential energy surfaces as a function of the β_2 and γ deformation parameters for the $^{186,188,190}\text{Hg}$ isotopes. The results are obtained with the Gogny-D1M interaction within the constrained Hartree-Fock-Bogoliubov approach and serve as a basis for the 5DCH calculations.

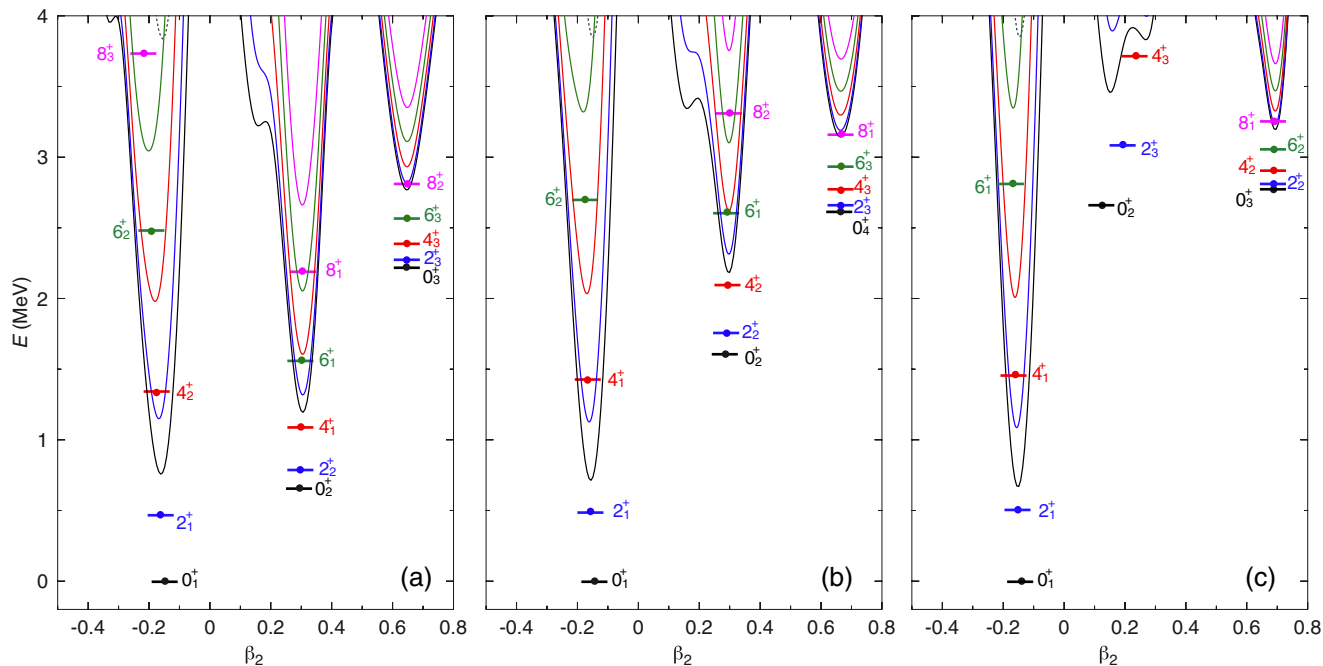


FIG. 10. Energy spectra obtained with axial SCCM calculations with the Gogny-D1S interaction for the (a) ^{186}Hg , (b) ^{188}Hg , and (c) ^{190}Hg isotopes. The energies are plotted at the mean value of the intrinsic quadrupole deformation of the corresponding collective wave functions. PNAMP energy curves as a function of β_2 are also plotted to guide the eye.

the excited states. At the same time, the SCCM calculation predicts a band crossing at $J^\pi = 6^+$ in ^{188}Hg in agreement with the observations, i.e., the members of the ND-prolate band become yrast at $J = 6, 8, 10$. Correct band crossing is also predicted for $^{186,190}\text{Hg}$. Regarding the level spacing of the two bands, the SCCM method reproduces better the properties of the ND-prolate band (band B), while the 5DCH approach provides a better description of the weakly deformed structure (band A). Due to the included triaxial degree of freedom, the 5DCH is able to predict a γ band (band C) appearing at

low excitation energy. Such a structure has not been observed in the experiments presented in this work, but it was first postulated in a β -decay study of Ref. [57] and then confirmed in Ref. [58], although the existing spin assignments are not firm.

Finally, a potential energy minimum corresponding to a superdeformed shape is predicted in both theoretical approaches. In this work, the superdeformed states were only obtained in SCCM calculations (band D). Indeed, in the 5DCH approach a two-center basis has to be adopted for

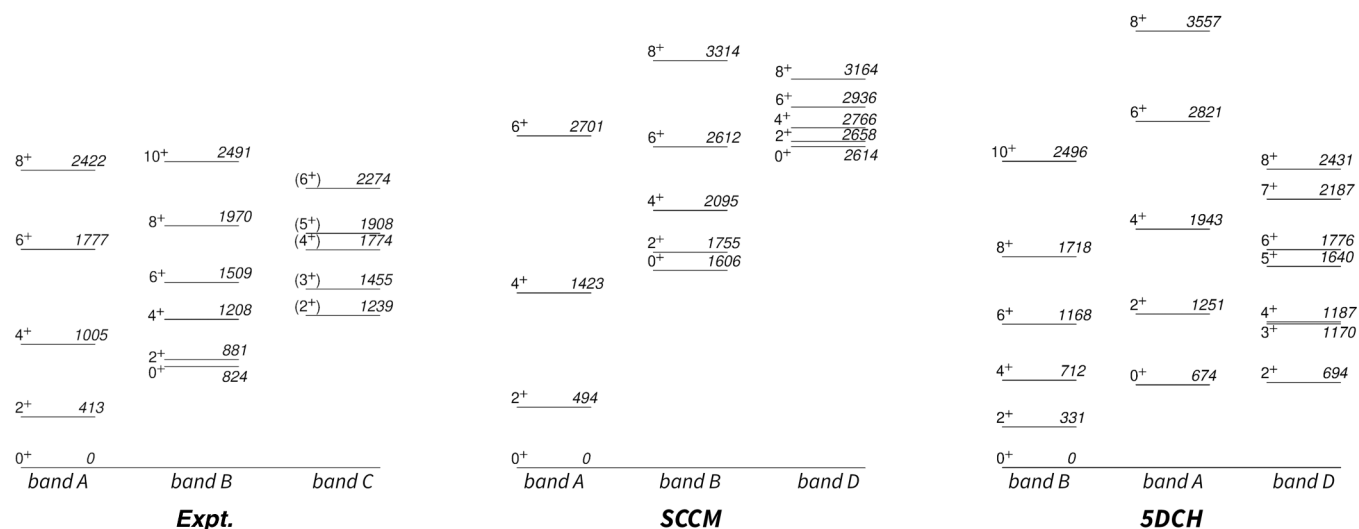


FIG. 11. Partial level scheme of ^{188}Hg , reporting the low-lying excited states. The experimental results are compared with the energy spectra predicted by the 5DCH and SCCM approaches.

diagonalizing the Bohr Hamiltonian in order to explore the highly deformed structure [56]. Such a structure has not been observed in ^{188}Hg , while it is known in the neighboring ^{189}Hg and ^{190}Hg [59–61].

The CWFs, i.e., the weights of the intrinsic quadrupole deformations in each nuclear state, are presented in Fig. 12 and Fig. 13 for the SCCM and 5DCH methods, respectively. For SCCM, those for states belonging to bands A, B, and D (see Fig. 11) are plotted, while for 5DCH the CWFs for band heads of bands A and B are shown. The SCCM calculations predict a rather constant deformation within each of the three calculated bands (oblate band A with $\beta_2 \approx -0.18$, normal-deformed prolate band B with $\beta_2 \approx 0.22$, and superdeformed band D with $\beta_2 \approx 0.65$). For the ground-state and ND bands, the deformation parameters from the SCCM calculations are in fair agreement with those estimated from the experimental results, assuming the rotational model (see Table II). The overlaps between the CWFs are negligible, which can be related to a very small mixing between the three structures and attributed to the imposition of axial symmetry in the calculations. An exploratory calculation with $N_{h.o} = 11$ including triaxial shapes for ^{188}Hg suggests a larger mixing between the oblatelike and ND prolatelike configurations along the γ degree of freedom.

The wave functions resulting from the 5DCH approach are much more spread on the (β_2, γ) plane and the distributions calculated for states belonging to the different structures present considerable overlaps, see Fig. 13. Due to the importance of the triaxial degree of freedom, it is impossible to refer to the two bands as “prolate” and “oblate”. The average β_2 deformation of states belonging to the band B, corresponding to the experimentally observed deformed band built on the 0_2^+ state in ^{188}Hg , slowly increases with spin starting from $\beta_2 = 0.2$ for the 0^+ state, which is in fair agreement with the β_2 deformation estimated from the experimental data. A gradual evolution from an almost maximally triaxial shape with $\gamma = 27^\circ$ for the 0^+ state towards a more prolate deformation higher up in the band is also predicted. Notably, the average γ deformation parameter for the states of spin $J \geq 4$ is about 15° , very close to the value derived from the experimental transition probabilities using the asymmetric rotor model (see Sec. IV). Interestingly, an average γ deformation parameter of about 15° was also obtained for the states belonging to band B in the exploratory SCCM calculations including the triaxial degree of freedom, but limited to $N_{h.o} = 11$. The average elongation parameter of states belonging to band A, corresponding to the experimental ground-state band in ^{188}Hg , is $\beta_2 \approx 0.25$ and remains constant within the band, while the triaxial parameter evolves from about $\gamma \approx 20^\circ$ towards maximum triaxiality. The states belonging to this oblatelike structure present strong admixtures of the $K = 2$ configuration, being as large as almost 50% for the 2_A^+ state.

Both calculations yield a similar picture of two structures with $|\beta_2| \approx 0.2$, coexisting at low excitation energy. The 5DCH calculations suggest that at low-spin the triaxial degree of freedom is important. Unfortunately, the precision of the experimentally determined quadrupole moment of the 2_1^+ state in ^{188}Hg , equal to $0.8_{-0.3}^{+0.5}$ eb [30] is insufficient to make a conclusion about the degree of triaxiality in this

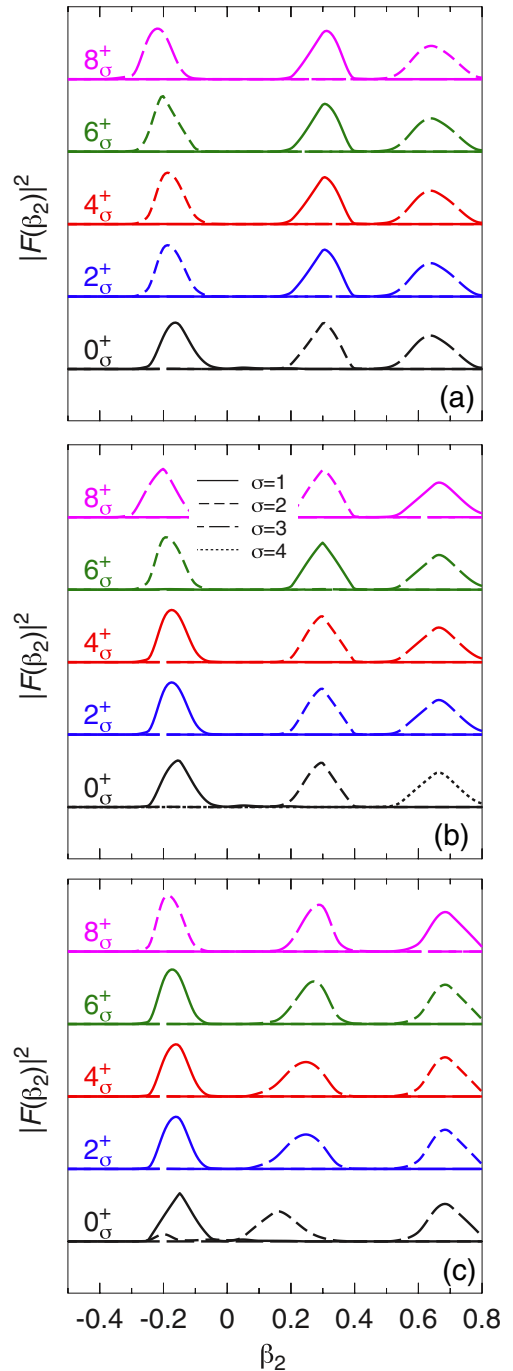


FIG. 12. Collective wave functions (CWF) obtained with axial SCCM calculations with the Gogny-D1S interaction for (a) ^{186}Hg , (b) ^{188}Hg , and (c) ^{190}Hg isotopes. The full, short-dashed, dashed, and dotted lines represent the first, second, third, and fourth excited state, respectively. Only CWFs for states belonging to the first three collective bands (oblate, ND, and SD prolate) are shown.

state. This value is compatible with both calculations: the SCCM calculations give $Q_s(2_A^+) = 1.3$ eb, while in the 5DCH calculations, which attribute a triaxial character to the 2_A^+ state, the spectroscopic quadrupole moment is $Q_s(2_A^+) = 0.5$ eb.

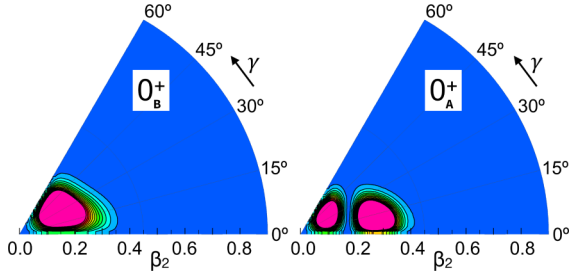


FIG. 13. Collective wave functions (CWF) as a function of the β_2 and γ deformation parameters for the 0_A^+ and 0_B^+ states, obtained with the Gogny-D1M interaction within the 5DCH framework.

Table II presents a comparison of the experimental reduced transition probabilities in ^{188}Hg with those calculated within the SCCM and 5DCH approaches. In order to facilitate the comparison, the 5DCH results for the ground-state band are reported next to those for the more deformed structure (band A), while those for the structure built on the 0_2^+ are listed next to those for the experimental weakly deformed ground-state band (band B).

The agreement for in-band transitions is reasonably good, with the transitions within the weakly deformed band (band A) described better by SCCM, while those in the more deformed structure (band B) are overestimated by both models, with the 5DCH results being closer to experimental values. In contrast, both models struggle to reproduce the experimentally observed interband transitions, predicting a relatively large mixing of the two structures, which rapidly decreases with the increasing spin (see Table III). In fact, the strength of the $2_2^+ \rightarrow 0_{g.s.}^+$ interband transition is slightly overestimated by the two calculations. The $B(E2; 6_1^+ \rightarrow 4_1^+)$ value, instead, is underestimated, with the one resulting from the SCCM approach being more than one order of magnitude smaller than the experimental value. This latter result can be interpreted as an underestimation of the possible mixing between the two bands, consistent with the negligible overlaps between the CWFs (Fig. 12).

For a more quantitative comparison, one can extract the mixing amplitudes α_{mix} [see Eq. (5)] for the 0^+ , 2^+ , and 4^+ states from the calculated $B(E2)$ transition probabilities

TABLE III. Average quadrupole moments (in eb) of the normal and intruder configurations as well as the mixing amplitudes α_{mix} for the $0_{g.s.}^+$, 2_1^+ , and 4_1^+ states extracted from the theoretical $B(E2)$ values from 5DCH and SCCM calculations using the two-band mixing model, compared with those deduced from experimental data (see text). Due to the bands swapping, for the 5DCH and SCCM ($N_{h.o.} = 11$) calculations the values are interchanged to facilitate a direct comparison with the experimental results.

| | $\alpha_{\text{mix}}(0_{g.s.}^+)$ | $\alpha_{\text{mix}}(2_1^+)$ | $\alpha_{\text{mix}}(4_1^+)$ | $ Q_0^{\text{n}} $ | $ Q_0^{\text{i}} $ |
|--------------------------|-----------------------------------|------------------------------|------------------------------|--------------------|--------------------|
| Expt. | 0.995 | 0.988 | 0.893 | 3.67(37) | 6.41(43) |
| 5DCH | 0.720 | 0.866 | 0.942 | 4.20 | 7.68 |
| SCCM ($N_{h.o.} = 11$) | 0.800 | 0.911 | 0.949 | 3.12 | 9.61 |
| SCCM ($N_{h.o.} = 17$) | 0.993 | 0.980 | 0.994 | 4.45 | 8.45 |

using the equations listed in Sec. V A of Ref. [45]. The values obtained using this approach from the experimental data and from the model calculations are reported in Table III. As expected, the mixing strengths for the 0^+ (48%) and 2^+ (25%) states obtained within the 5DCH approach are much larger than those for the SCCM calculations (1.4% and 4%, respectively), which better reproduce the values obtained using the experimental data. In contrast, the large mixing strength for the 4^+ states deduced from the experimental data (20%) is better reproduced by the 5DCH calculations, which predict 11% admixture in contrast with 1.2% from SCCM. This approach also provides the quadrupole moments of the normal and intruder bands, which remain constant as a function of the spin. The $|Q_0^{\text{i}}|$ values extracted from the theoretical calculations are compatible with those deduced from the experimental $B(E2)$ values. For the intruder band, instead, both SCCM and 5DCH models overestimate the value of $|Q_0^{\text{i}}|$, consistent with the overestimation of $B(E2)$ values in this band (see Table II).

Finally, the underlying shell structure of the three collective bands can be also analyzed within the SCCM framework. The relevant spherical shells that are needed to describe such states can be qualitatively identified by Nilsson-like orbitals. These orbitals are computed self-consistently for each nucleus with HFB states obtained along the quadrupole degree of freedom. As an example, the evolution of the orbitals as a function of the deformation, β_2 , is plotted for the ^{188}Hg isotope in Fig. 14. The Fermi energies for protons and neutrons are also shown. The relevant regions, where the CWF are peaked (i.e., the minima of the energy surfaces), are marked by a gray band in the figure. In the oblate minimum, we see that the orbitals close to the Fermi energy are $3s_{1/2}$, $0h_{11/2}$, and $0h_{9/2}$ for protons and $0h_{9/2}$, $1f_{7/2}$, $0i_{13/2}$, $2p_{3/2}$, and $1f_{5/2}$ for neutrons. For the ND configuration, the $1d_{5/2}$ and the $1f_{7/2}$ for protons and the $0g_{9/2}$ for neutrons also play a role. Finally, for the SD band, the $0i_{11/2}$ and negative parity orbitals above $N = 126$ are also crossing the neutron Fermi energy. This picture shows the complexity of the single-particle structure of these heavy nuclei. We compute the occupation numbers of spherical orbitals with each individual SCCM wave function in the three isotopes studied here following the method developed in Ref. [62]. To simplify the discussion, we define a proton core of $Z = 82$ that encompasses the $0s$, $0p$, $1s-0d$, $1p-0f$, $2s-1d-0g$, and $0h_{11/2}$ spherical orbitals, and a neutron core of $N = 100$ that includes the orbitals listed above plus the $0h_{9/2}$ and $1f_{7/2}$ neutron levels. Using such cores, the ^{188}Hg isotope in a normal filling approximation should correspond to $2h-0p$ (protons) and $0h-8p$ (neutrons), respectively. However, the results obtained for the oblate, ND, and SD bands are $4.0h-2.0p$, $8.1h-6.1p$, and $9.0h-7.0p$ for protons, and $5.4h-13.4p$, $7.7h-15.7p$, and $8.3h-16.3p$ for neutrons, respectively. Similar configurations are also obtained for the other two isotopes calculated here. Those can be compared with the results of the Monte Carlo shell-model (MCSM) calculations for lighter Hg isotopes [2,63], which predict two configurations, one more deformed (oblate, being the ground state in even-odd nuclei) than the other (prolate, ground state of even-even nuclei). For the less deformed configuration, the number of protons above the $Z = 82$ gap is small and the

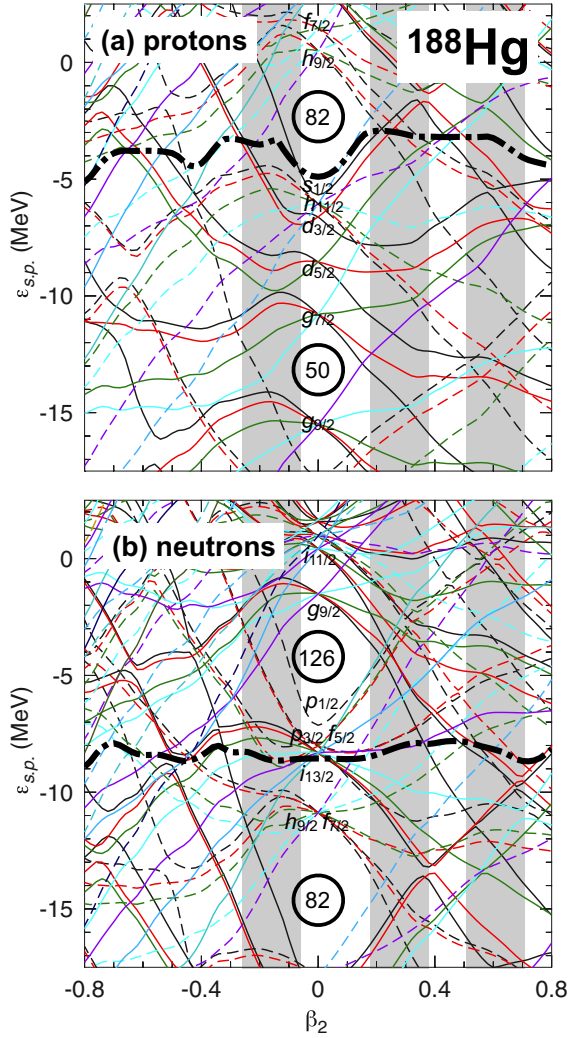


FIG. 14. Single-particle energies for (a) protons and (b) neutrons as a function of the deformation β_2 calculated for ^{188}Hg with the Gogny D1S interaction. Dashed (continuous) lines represent negative (positive) parity states and the thick dashed-dotted lines show the Fermi energy. The shaded areas correspond to the position of the three minima in the energy surface shown in Fig. 8.

number of neutrons in the $i_{13/2}$ shell steadily increases with N in even-even isotopes as expected for a nearly spherical configuration (e.g., for the ^{186}Hg ground state). However, for the more prolate-deformed configurations larger occupancies of protons above $Z = 82$ and a constant number of neutrons in the $i_{13/2}$ orbital are obtained. The latter is observed because the single-particle levels with smaller (larger) Nilsson- Ω quantum numbers coming from this orbital are well below (above) the neutron Fermi level at prolate deformations and their occupancies are saturated. These two configurations found in the MCSM calculations would correspond to the oblate and ND states obtained with the SCCM method and we observe a similar behavior of the occupation numbers obtained with both methods. However, the SCCM calculations predict larger deformations for oblate and ND states, as well as the numbers of particles above $Z = 82$ and the neutron $i_{13/2}$ orbital. In addition, it is likely that the SD states, not found

in the MCSM calculations, are beyond the (large) valence space used in those calculations. These results show again the complexity of the single-particle structure driven by the deformation of the system.

V. CONCLUSIONS

The nuclear structure of the neutron-deficient mercury isotope ^{188}Hg was investigated via lifetime measurements at the Laboratori Nazionali di Legnaro. In order to control a possible contamination of the ^{188}Hg data by other reaction channels, two different fusion-evaporation reactions were used for this study and, thanks to the powerful capabilities of both GALILEO and Neutron Wall arrays, a clear identification of the channel of interest was possible.

Using the RDDS technique, the lifetimes of the states up to spin $16\hbar$ were measured and the results obtained for the 2_1^+ and 4_1^+ states are in agreement with the values reported in literature. Thanks to the new results for both low- and high-lying states, the deformation of the ground-state band and of the intruder structure was estimated from the experimental data, assuming two-band mixing and two different rotational models. These models provide a similar interpretation of the structures: the ground-state band has a quadrupole deformation of $\beta_2 \approx 0.13$, while the intruder one has $\beta_2 \approx 0.22$. Moreover, the lifetimes of the 14_1^+ and 16_1^+ excited states highlighted the presence of an almost spherical structure above the 12_1^+ isomer.

In view of the new results, two state-of-the-art beyond-mean-field calculations were performed for the even-mass $^{186-190}\text{Hg}$ nuclei using the symmetry-conserving configuration-mixing approach limited to axial shapes and the five-dimensional collective Hamiltonian including the triaxial degree of freedom. Both calculations yield a similar picture of two structures with $|\beta_2| \approx 0.2$, coexisting at low excitation energy, but predict different relative positions of the two bands and their mixing. The underlying shell structure of the collective bands was analyzed within the SCCM framework, identifying the relevant spherical shells, necessary to describe such structures. For ^{188}Hg the comparison between the theoretical predictions and the experimental results confirmed the proposed interpretation of both the intruder and ground-state bands.

In contrast with other beyond-mean-field calculations, the SCCM approach predicts the presence of shape coexistence also in ^{190}Hg , with the band head of the SD structure mixing with those of the ND prolate and oblate bands. Clearly, further experimental studies of ^{190}Hg are required to verify these predictions. The mixing amplitudes for the 0^+ states in $^{180-188}\text{Hg}$ deduced from level energies and $E2$ transition strengths differ from those obtained from α -decay hindrance factors. In this context, measurements of $\rho^2(E0)$ between the coexisting structures are called for, as they would provide a direct measure of the degree of their mixing.

ACKNOWLEDGMENTS

The authors would like to thank the GALILEO collaboration. Special thanks go to the INFN-LNL technical staff

for their help and the good quality beam and to Massimo Loriggiola for the extended work on the Gd plunger targets. We acknowledge the numerical calculations of S. Hilaire. This paper owes much to the collaboration with P. E. Garrett. This work was partially supported by the Espace de Structure Nucléaire Théorique (CEA/DSM-DAM). The work of T.R.R. was supported by the Spanish MICINN under Grant

No. PGC2018-094583-B-I00. The work was also supported (P.R.J. and P.K.) by the German BMBF under Contract No. 05P18RDFN9, (G.J.) by the National Science Centre Poland (NCN) under the Grant No. 2017/25/B/ST2/01569. A.G. acknowledges the support of the Fondazione Cassa di Risparmio Padova e Rovigo under the project CONPHYT, starting grant in 2017.

- [1] T. Kühl, P. Dabkiewicz, C. Duke, H. Fischer, H. J. Kluge, H. Kremmling, and E.-W. Otten, *Phys. Rev. Lett.* **39**, 180 (1977).
- [2] B. Marsh, T. Day Goodacre, S. Sels, Y. Tsunoda, B. Andel, A. N. Andreyev, N. A. Althubiti, D. Atanasov, A. E. Barzakh, J. Billowes *et al.*, *Nat. Phys.* **14**, 1163 (2018).
- [3] A. Ansari, *Phys. Rev. C* **33**, 321 (1986).
- [4] P. R. John, V. Modamio, J. J. Valiente-Dobón, D. Mengoni, S. Lunardi, T. R. Rodríguez, D. Bazzacco, A. Gadea, C. Wheldon, T. Alexander *et al.*, *Phys. Rev. C* **90**, 021301 (2014).
- [5] P. R. John, J. J. Valiente-Dobón, D. Mengoni, V. Modamio, S. Lunardi, D. Bazzacco, A. Gadea, C. Wheldon, T. R. Rodríguez, T. Alexander *et al.*, *Phys. Rev. C* **95**, 064321 (2017).
- [6] A. N. Andreyev, M. Huyse, P. Van Duppen, L. Weissman, D. Ackermann, J. Gerl, F. P. Hessberger, S. Hofmann, A. Kleinböhl, G. Münzenberg *et al.*, *Nature (London)* **405**, 430 (2000).
- [7] P. R. Rahkila, D. G. Jenkins, J. Pakarinen, C. Gray-Jones, P. T. Greenlees, U. Jakobsson, P. Jones, R. Julin, S. Juutinen, S. Ketelhut *et al.*, *Phys. Rev. C* **82**, 011303(R) (2010).
- [8] J. Bonn, G. Huber, H. Kluge, L. Kluger, and E. Otten, *Phys. Lett. B* **38**, 308 (1972).
- [9] I. Angeli and K. Marinova, *At. Nucl. Data Tables* **99**, 69 (2013).
- [10] M. R. Bhat, in *Nuclear Data for Science and Technology*, edited by S. M. Qaim (Springer, Berlin, 1992), p. 817.
- [11] J. D. Cole, J. H. Hamilton, A. V. Ramayya, W. G. Nettles, H. Kawakami, E. H. Spejewski, M. A. Ijaz, K. S. Toth, E. L. Robinson, K. S. R. Sastry *et al.*, *Phys. Rev. Lett.* **37**, 1185 (1976).
- [12] J. H. Hamilton, A. V. Ramayya, E. L. Bosworth, W. Lourens, J. D. Cole, B. Van Nooijen, G. Garcia-Bermudez, B. Martin, B. N. S. Rao, H. Kawakami *et al.*, *Phys. Rev. Lett.* **35**, 562 (1975).
- [13] J. Wauters, N. Bijnens, H. Folger, M. Huyse, H. Y. Hwang, R. Kirchner, J. von Schwarzenberg, and P. Van Duppen, *Phys. Rev. C* **50**, 2768 (1994).
- [14] P. Joshi, E. Zganjar, D. Rupnik, S. Robinson, P. Mantica, H. Carter, J. Kormicki, R. Gill, W. Walters, C. Bingham *et al.*, *Int. J. Mod. Phys. E* **3**, 757 (1994).
- [15] G. D. Dracoulis, *Phys. Rev. C* **49**, 3324 (1994).
- [16] L. P. Gaffney, M. Hackstein, R. D. Page, T. Grahn, M. Scheck, P. A. Butler, P. F. Bertone, N. Bree, R. J. Carroll, M. P. Carpenter *et al.*, *Phys. Rev. C* **89**, 024307 (2014).
- [17] R. D. Page, A. N. Andreyev, D. R. Wiseman, P. A. Butler, T. Grahn, P. T. Greenlees, R.-D. Herzberg, M. Huyse, G. D. Jones, P. M. Jones *et al.*, *Phys. Rev. C* **84**, 034308 (2011).
- [18] E. Rapisarda, A. N. Andreyev, S. Antalic, A. Barzakh, T. E. Cocolios, I. G. Darby, R. D. Groote, H. D. Witte, J. Diriken, J. Elseviers *et al.*, *J. Phys. G: Nucl. Part. Phys.* **44**, 074001 (2017).
- [19] J. D. Cole, A. V. Ramayya, J. H. Hamilton, H. Kawakami, B. van Nooijen, W. G. Nettles, L. L. Riedinger, F. E. Turner, C. R. Bingham, H. K. Carter *et al.*, *Phys. Rev. C* **16**, 2010 (1977).
- [20] M. Scheck, P. A. Butler, L. P. Gaffney, N. Bree, R. J. Carroll, D. Cox, T. Grahn, P. T. Greenlees, K. Hauschild, A. Herzan *et al.*, *Phys. Rev. C* **83**, 037303 (2011).
- [21] C. Müller-Gatermann, A. Dewald, C. Fransen, K. Auranen, H. Badran, M. Beckers, A. Blazhev, T. Braunroth, D. M. Cullen, G. Fruet *et al.*, *Phys. Rev. C* **99**, 054325 (2019).
- [22] T. Grahn, A. Petts, M. Scheck, P. A. Butler, A. Dewald, M. B. Gomez Hornillos, P. T. Greenlees, A. Görgen, K. Helariutta, J. Jolie *et al.*, *Phys. Rev. C* **80**, 014324 (2009).
- [23] M. Scheck, T. Grahn, A. Petts, P. A. Butler, A. Dewald, L. P. Gaffney, M. B. Gomez Hornillos, A. Görgen, P. T. Greenlees, K. Helariutta *et al.*, *Phys. Rev. C* **81**, 014310 (2010).
- [24] N. Rud, D. Ward, H. R. Andrews, R. L. Graham, and J. S. Geiger, *Phys. Rev. Lett.* **31**, 1421 (1973).
- [25] D. Proetel, R. M. Diamond, and F. S. Stephens, *Phys. Lett. B* **48**, 102 (1974).
- [26] W. Ma, A. Ramayya, J. Hamilton, S. Robinson, J. Cole, E. Zganjar, E. Spejewski, R. Bengtsson, W. Nazarewicz, and J.-Y. Zhang, *Phys. Lett. B* **167**, 277 (1986).
- [27] B. Olaizola, A. B. Garnsworthy, F. A. Ali, C. Andreoiu, G. C. Ball, N. Bernier, H. Bidaman, V. Bildstein, M. Bowry, R. Caballero-Folch *et al.*, *Phys. Rev. C* **100**, 024301 (2019).
- [28] A. Esmaylzadeh, L. M. Gerhard, V. Karayonchev, J.-M. Régis, J. Jolie, M. Bast, A. Blazhev, T. Braunroth, M. Dannhoff, F. Dunkel *et al.*, *Phys. Rev. C* **98**, 014313 (2018).
- [29] N. Bree, K. Wrzosek-Lipska, A. Petts, A. Andreyev, B. Bastin, M. Bender, A. Blazhev, B. Bruyneel, P. A. Butler, J. Butterworth *et al.*, *Phys. Rev. Lett.* **112**, 162701 (2014).
- [30] K. Wrzosek-Lipska, K. Rezykina, N. Bree, M. Zielińska, L.P. Gaffney, A. Petts, A. Andreyev, B. Bastin, M. Bender, A. Blazhev *et al.*, *Eur. Phys. J. A* **55**, 130 (2019).
- [31] C. Praharaj and S. Khadkikar, *J. Phys. G: Nucl. Phys.* **6**, 241 (1980).
- [32] T. Nikšić, D. Vretenar, P. Ring, and G. A. Lalazissis, *Phys. Rev. C* **65**, 054320 (2002).
- [33] C. Signorini, G. Bezzon, F. Cervellera, P. Spolaore, and R. Ricci, *Nucl. Instrum. Methods Phys. Res. A* **220**, 30 (1984).
- [34] A. Dainelli, G. Bassato, A. Battistella, M. Bellato, A. Beltramin, L. Bertazzo, G. Bezzon, G. Bisoffi, L. Boscagli, S. Canella *et al.*, *Nucl. Instrum. Methods Phys. Res. A* **382**, 100 (1996).
- [35] D. Testov, J. J. Valiente-Dobón, D. Mengoni, F. Recchia, A. Goasduff, A. Boso, S. M. Lenzi, G. de Angelis, S. Bakes, C. Boiano *et al.*, [arXiv:1903.01296](https://arxiv.org/abs/1903.01296).
- [36] Ö. Skeppstedt, H. Roth, L. Lindström, R. Wadsworth, I. Hibbert, N. Kelsall, D. Jenkins, H. Grawe, M. Górska, M. Moszyński *et al.*, *Nucl. Instrumentation Method Phys. Res. A* **421**, 531 (1999).
- [37] I. Zanon, M. Siciliano, P. R. John, A. Goasduff, D. Bazzacco, D. Ashad, G. Benzoni, B. Birkenbach, T. Braunroth, A. Boso

- et al.*, INFN-LNL Report 251, 62 (2018), http://www.lnl.infn.it/~annrep/read_ar/2017/contributions/pdfs/062_B_24_B019.pdf.
- [38] I. Zanon, M. Siciliano, P. R. John, and A. Goasduff, *Nuovo Cimento C* **42**, 109 (2019).
- [39] A. Dewald, O. Möller, and P. Petkov, *Prog. Part. Nucl. Phys.* **67**, 786 (2012).
- [40] C. Müller-Gatermann, F. von Spee, A. Goasduff, D. Bazzacco, M. Beckers, T. Braunroth, A. Boso, P. Cocconi, G. de Angelis, A. Dewald *et al.*, *Nucl. Instrum. Methods A* **920**, 95 (2019).
- [41] B. Saha, *Napatau or Tk-Lifetime-Analysis* (Institute for Nuclear Physics, India, 2003).
- [42] F. Kondev, S. Juutinen, and D. Hartley, *Nucl. Data Sheets* **150**, 1 (2018).
- [43] P. Petkov, J. Gableske, O. Vogel, A. Dewald, P. von Brentano, R. Krücken, R. Peusquens, N. Nicolay, A. Gizon, J. Gizon *et al.*, *Nucl. Phys. A* **640**, 293 (1998).
- [44] G. Lane, G. Dracoulis, A. Byrne, S. Anderssen, P. Davidson, B. Fabricius, T. Kibédi, A. Stuchbery, and A. Baxter, *Nucl. Phys. A* **589**, 129 (1995).
- [45] E. Clément, A. Görgen, W. Korten, E. Bouchez, A. Chatillon, J.-P. Delaroche, M. Girod, H. Goutte, A. Hüerstel, Y. Le Coz *et al.*, *Phys. Rev. C* **75**, 054313 (2007).
- [46] J. Egidio, *Phys. Scr.* **91**, 073003 (2016).
- [47] L. Robledo, T. R. Rodríguez, and R. Rodríguez-Guzmán, *J. Phys. G: Nucl. Part. Phys.* **46**, 013001 (2018).
- [48] J.-P. Delaroche, M. Girod, J. Libert, H. Goutte, S. Hilaire, S. Péru, N. Pillet, and G. F. Bertsch, *Phys. Rev. C* **81**, 014303 (2010).
- [49] T. R. Rodríguez and J. L. Egidio, *Phys. Rev. C* **81**, 064323 (2010).
- [50] T. R. Rodríguez, *Phys. Rev. C* **90**, 034306 (2014).
- [51] S. Goriely, S. Hilaire, M. Girod, and S. Péru, *Phys. Rev. Lett.* **102**, 242501 (2009).
- [52] J. Dechargé and D. Gogny, *Phys. Rev. C* **21**, 1568 (1980).
- [53] J. Berger, M. Girod, and D. Gogny, *Comput. Phys. Commun.* **63**, 365 (1991).
- [54] M. Anguiano, J. Egidio, and L. Robledo, *Nucl. Phys. A* **696**, 467 (2001).
- [55] T. R. Rodríguez, A. Arzhanov, and G. Martínez-Pinedo, *Phys. Rev. C* **91**, 044315 (2015).
- [56] J. Delaroche, M. Girod, J. Libert, and I. Deloncle, *Phys. Lett. B* **232**, 145 (1989).
- [57] C. Bourgeois, M. Bouet, A. Caruette, A. Ferro, R. Foucher, J. Fournet, A. Höglund, L. Kotfila, G. Landois, C. Liang *et al.*, *J. Phys. France* **37**, 49 (1976).
- [58] J. D. Cole, J. H. Hamilton, A. V. Ramayya, W. Lourens, B. van Nooijen, H. Kawakami, L. A. Mink, E. H. Spejewski, H. K. Carter, R. L. Mlekodaj *et al.*, *Phys. Rev. C* **30**, 1267 (1984).
- [59] M. Drigert, M. Carpenter, R. Janssens, E. Moore, I. Ahmad, P. Fernandez, T. Khoo, F. Wolfs, I. Bearden, P. Benet *et al.*, *Nucl. Phys. A* **530**, 452 (1991).
- [60] I. G. Bearden, R. V. F. Janssens, M. P. Carpenter, E. F. Moore, I. Ahmad, A. M. Baxter, P. Benet, P. J. Daly, M. W. Drigert, P. B. Fernandez *et al.*, *Z. Phys. A: Hadrons Nucl.* **341**, 491 (1992).
- [61] I. Bearden, R. Janssens, M. Carpenter, E. Moore, I. Ahmad, P. Daly, R. Mayer *et al.*, *Nucl. Phys. A* **576**, 441 (1994).
- [62] T. R. Rodríguez, A. Poves, and F. Nowacki, *Phys. Rev. C* **93**, 054316 (2016).
- [63] S. Sels, T. Day Goodacre, B. A. Marsh, A. Pastore, W. Ryssens, Y. Tsunoda, N. Althubiti, B. Andel, A. N. Andreyev, D. Atanasov *et al.*, *Phys. Rev. C* **99**, 044306 (2019).